

# Summertime climate response to mountain pine beetle disturbance in British Columbia

H. Maness<sup>1,2\*</sup>, P. J. Kushner<sup>1</sup> and I. Fung<sup>2</sup>

**The present mountain pine beetle infestation in forests in British Columbia ranks among the largest ecological disturbances recorded in Canada so far. These recent outbreaks are thought to have been favoured by large-scale climatic shifts, and may foreshadow outbreaks of a similar magnitude in North American forests over the coming decades. The associated forest dieback could result in substantial shifts in evapotranspiration and albedo, thereby altering the local surface energy balance, and in turn regional temperature and climate. Here we quantify the impact of the Canadian pine beetle disturbance on the local summertime surface energy budget, using measurements of evapotranspiration, albedo and surface temperature, obtained primarily through remote sensing. We show that over the 170,000 km<sup>2</sup> of affected forest, the typical decrease in summertime evapotranspiration is 19%. Changes to the absorbed short-wave flux are negligible, in comparison. As a result, outgoing sensible and radiative heat fluxes increased by 8% and 1%, respectively, corresponding to a typical increase in surface temperature of 1 °C. These changes are comparable to those observed for other types of disturbance, such as wildfire, and may have secondary consequences for climate, including modifications to circulation, cloud cover and precipitation.**

Over the past decade, mountain pine beetle attacks in British Columbia have impacted nearly 20% of the total provincial area<sup>1</sup> (or 170,000 km<sup>2</sup>; Fig. 1). Similarly unprecedented levels of beetle outbreaks are also claiming large forested areas of the western United States<sup>2</sup>, and there is mounting evidence that these recent changes in outbreak rates are favoured by large-scale climatic shifts<sup>3</sup>. Indeed, outbreak frequency and geographic extent are expected to be markedly affected by global warming<sup>4</sup>. A recent study combining regional climate projections with an empirical model for spruce beetle development, for example, suggests that boreal forests across central Canada that are unthreatened at present may be potentially converted to regions of high outbreak probability by the turn of the century<sup>5</sup>. Such continental-scale outbreaks are expected to have substantial consequences for the global carbon budget<sup>6</sup>.

Resulting changes to the surface energy balance may also present important effects for regional climate. Research is ongoing to document and understand changes at the local level<sup>7–9</sup>; however, the larger-scale impact has remained largely unstudied<sup>10</sup>, especially during the growing season. Qualitatively, we expect that throughout the growing season, significant forest mortality leads to decreased canopy transpiration. For affected stands, incoming solar radiation previously spent evaporating water now heats the surface, elevating local surface temperatures. Convective transport of sensible heat also probably accounts for some fraction of the excess outgoing energy flux. Ultimately, this change to the surface energy balance may potentially alter the atmospheric boundary layer, with regional consequences for cloud formation and precipitation.

Here, we provide a first attempt to quantify surface energy budget impacts of ecological disturbance on the regional scale. We use publicly available data products together with previously published measurements and simple biophysical modelling in an effort to retrospectively diagnose post-disturbance changes. We place bounds on the climatic responses of surface temperature and turbulent heat and moisture fluxes that can be compared with simulations. Our results indicate that ecological disturbance can

have a significant effect on the surface energy balance, with typical changes to latent, sensible and radiative heat fluxes of –19%, 8% and 1%, respectively. These shifts may be sufficient to drive further changes in climate, potentially impacting secondary processes, such as circulation, cloud formation and precipitation.

## Observed post-disturbance changes to the energy balance

As orientation, Fig. 2 shows time series for several variables at the 1-km scale, averaged over multiple pixels and segregated by the degree of mortality. Figure 2a shows cumulative volumetric forest mortality,  $\Delta\Sigma$ , taken from forest survey data. Figure 2b,c shows Moderate Resolution Imaging Spectroradiometer (MODIS) June–July–August seasonal averages for evapotranspiration,  $E$ , and the day–night temperature difference,  $T_{11} - T_{21}$ , where the subscripts denote local observation times, which are 11:30 and 21:30 to within one hour for all pixels. Before averaging, each individual time series was shifted in time according to the year of maximum forest surface density change between 2000 and 2010 (see Methods).

The time series in Fig. 2 show post-disturbance changes consistent with expectations. Specifically, decreases in evapotranspiration and increases in daytime relative to night-time temperature are observed. Furthermore, the magnitude of change depends on the level of mortality, with severely affected regions showing larger changes than areas with comparatively modest levels of mortality. The observed changes in  $E$  and  $T_{11} - T_{21}$  thus represent highly localized shifts, with their significance for climate lying in the large magnitude of affected area.

Although Fig. 2 clearly shows a post-disturbance decrease in evapotranspiration, the a priori reliability of this result is questionable. Unlike surface temperature, which is closely linked to observed long-wave radiances, evapotranspiration is not directly observed. Its retrieval instead relies on land surface variables that are directly observable, coupled with a model describing how the observed surfaces deliver water to the atmosphere. The optimal algorithm for describing all types of surface remains an area of

<sup>1</sup>Department of Physics, University of Toronto, Toronto, Ontario, M5S 1A7, Canada, <sup>2</sup>Department of Earth and Planetary Sciences, University of California at Berkeley, Berkeley, California 94720, USA. \*e-mail: maness@berkeley.edu.

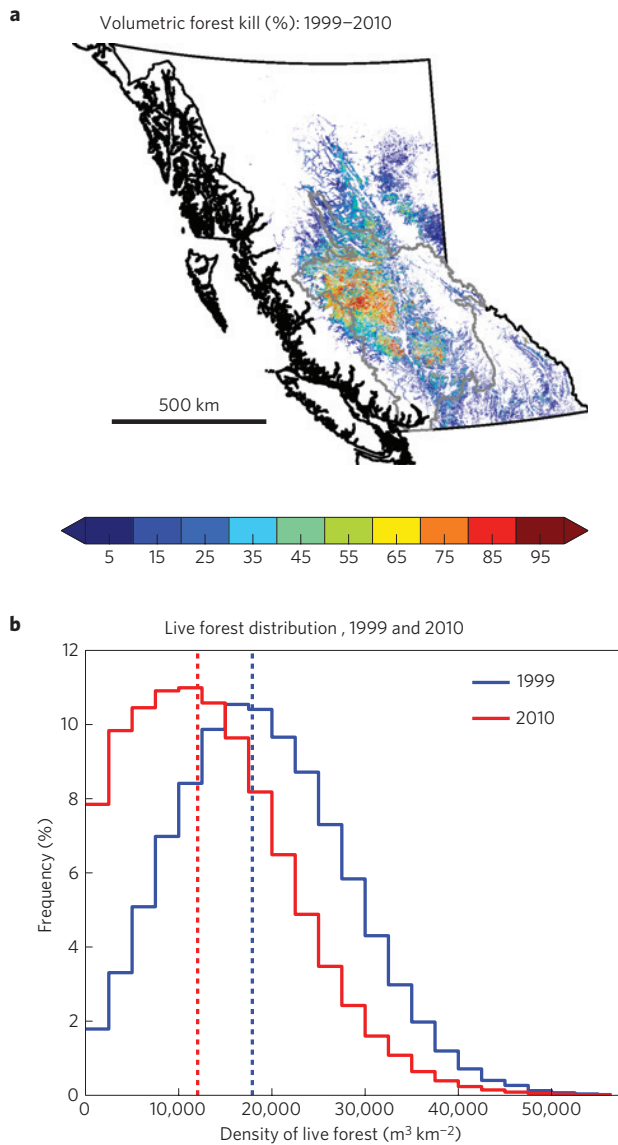


**Figure 1 | Forest mortality between 1999 and 2010, generated from data published by the British Columbia Forest Ministry<sup>1</sup>.** **a**, Fractional volumetric mortality, with the Fraser River Basin in grey. **b**, Pre- and post-disturbance histograms of live forest density. The blue and red dashed lines indicate the median densities in 1999 and 2010, respectively. The difference in the median values is  $\Delta\Sigma = 6,000 \text{ m}^3 \text{ km}^{-2}$ .

ongoing research; at present, different approaches to the retrieval of evapotranspiration often result in estimates for the same region that differ by as much as a factor of several<sup>11,12</sup>. The large spatial extent of the disturbance and the retrospective nature of our investigation prohibit a fully exhaustive validation. Our approach is instead to gauge the extent to which available data constrain the observed disturbance and tell a self-consistent story. The scale of the MODIS evapotranspiration in British Columbia and its partitioning between transpiration and evaporation are supported by three lines of evidence described in the following three sections.

#### MODIS evapotranspiration satisfies a closed water balance.

Figure 3 shows monthly time series for MODIS evapotranspiration averaged over the 217,000 km<sup>2</sup> Fraser River Basin within which most of the infestation is contained (Fig. 1). Also shown is the evapotranspiration inferred by combining Global Precipitation Climatology Centre (GPCC) precipitation data, Water Survey of

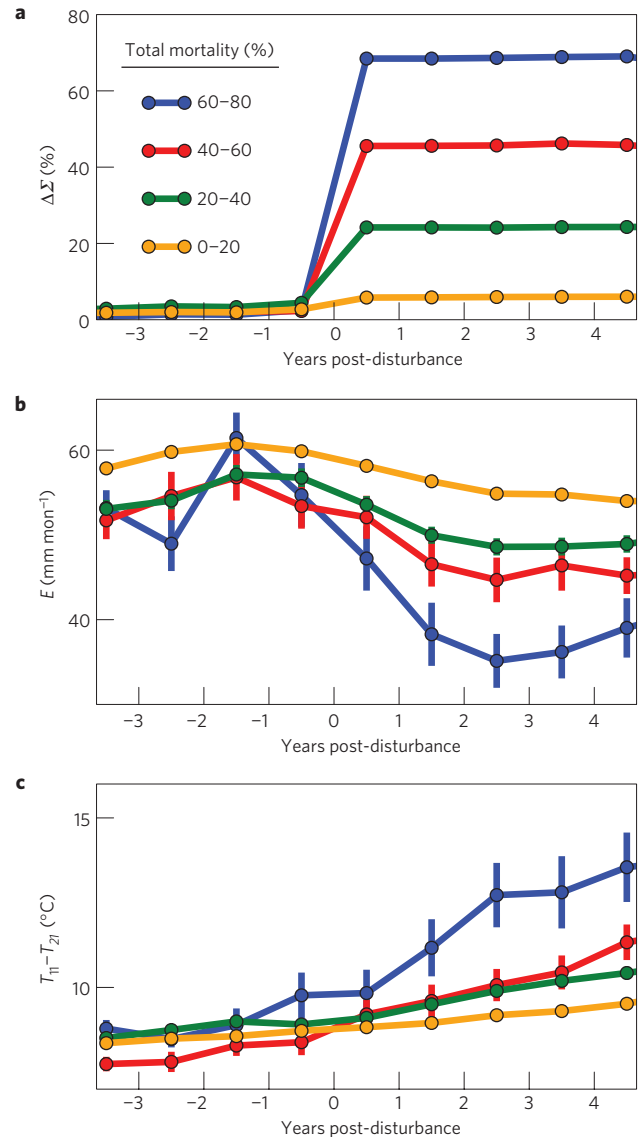


**Figure 2 | Multi-pixel average time series for several summertime variables at the 1-km scale, segregated by the degree of forest mortality.** **a**, Cumulative volumetric forest mortality ( $\Delta\Sigma$ ). **b**, MODIS evapotranspiration ( $E$ ). **c**, The MODIS-observed day-night temperature difference ( $T_{11} - T_{21}$ ). Error bars reflect  $2\sigma$  Poisson counting uncertainties.

Canada (WSC) river gauge data and Gravity Recovery and Climate Experiment (GRACE) storage data. The red and blue horizontal lines further indicate the average summertime evapotranspiration calculated from the MODIS and GPCC/WSC/GRACE time series, respectively. Translucent bars indicate the error in these climatologies, assuming measurements in consecutive years are independent.

Within the calculated errors, MODIS average summertime evapotranspiration ( $58 \pm 2 \text{ mm mon}^{-1}$ ) agrees with that inferred from water balance ( $56 \pm 5 \text{ mm mon}^{-1}$ ). Thus, assuming the Fraser Basin average is representative of the beetle-killed forests contained within it, these measurements set an upper limit to the amount of transpiration that can be lost post-disturbance.

#### Stand-level measurements support MODIS evapotranspiration.

Figure 4a shows all available MODIS data binned in terms of  $\Sigma_0$ , the volumetric forest surface density pre-disturbance, and  $f_{\text{live}}$ , the fraction of living trees. The binning is such that an

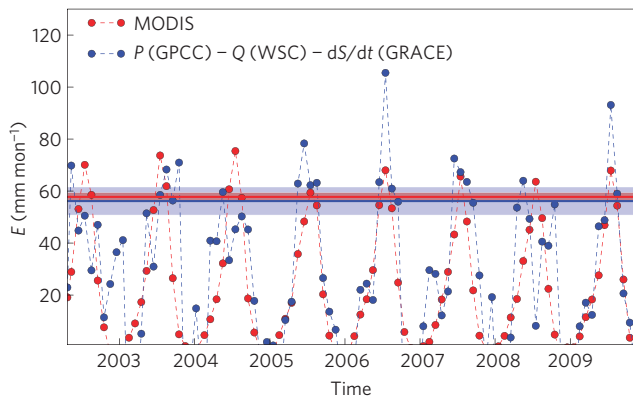


**Figure 3 | Fraser River Basin evapotranspiration time series for MODIS compared with that inferred from water balance.** The red and blue horizontal lines indicate the average summertime evapotranspiration calculated from the two time series, with translucent bars (corresponding colours) indicating the error in these climatologies, assuming measurements in consecutive years are independent.

approximately equal number of unbinned data points contribute to each binned data point.

Figure 4a reveals that when virtually all trees are dead (black line,  $f_{live} = 0.0-0.1$ ), MODIS evapotranspiration is independent of the initial forest surface density. Tree transpiration in this case is near zero and the near-constant value of 35–40 mm mon<sup>-1</sup> can be attributed to evaporation. This estimate is in line with the upper limit placed by summertime precipitation (see Methods). In contrast to the case in which all trees are dead, Fig. 4a shows that when virtually all trees are live (red line,  $f_{live} = 0.9-1.0$ ), MODIS evapotranspiration initially increases with forest surface density and then asymptotes to a maximal value for  $\Sigma_0 \gtrsim 20,000 \text{ m}^3 \text{ km}^{-2}$ . This behaviour is consistent with a scenario in which transpiration is limited by net radiation to the surface. Indeed, MODIS actual evapotranspiration tends to be well correlated with potential evapotranspiration (the theoretical maximum evapotranspiration possible based on available energy); the median correlation coefficient for the individual time series is  $r = 0.6$ .

Assuming tree transpiration is limited by net radiation, evaporation from soil and vegetation is water-limited, and dead trees retain their needles for the first several years following attack<sup>13</sup>, a simple model for forest evapotranspiration can be written as:

$$E = E_{canopy,max} f_{live} (1 - e^{-\Sigma_0 / \Sigma_{crown}}) + E_{evap} \quad (1)$$

Here,  $E_{canopy,max}$  is the maximum canopy transpiration corresponding to a fully live canopy and a fully shaded soil surface,  $\Sigma_{crown}$  is the forest density at which the optical depth to the forest floor is unity and  $E_{evap}$  is soil and vegetation evaporation. Equation (1) is derived in the Supplementary Information.

Figure 4b shows a nonlinear least-squares fit of equation (1) to the binned data. The fitted parameters are  $\Sigma_{crown} = 12,000 \pm 1,000 \text{ m}^3 \text{ km}^{-2}$ ,  $E_{canopy,max} = 37 \pm 1 \text{ mm mon}^{-1}$  and  $E_{evap} = 35.1 \pm 0.3 \text{ mm mon}^{-1}$ . To test the MODIS results, we independently estimate  $\Sigma_{crown}$ ,  $E_{canopy,max}$  and  $E_{evap}$  using previously reported *in situ* measurements. Assuming the maximum optical depth through a single tree is of order unity, the first parameter can be estimated from simple geometric arguments:  $\Sigma_{crown} \sim 13,000 \text{ m}^3 \text{ km}^{-2}$  (see Supplementary Information); this estimate agrees with the value fitted to the MODIS data to within the fitted error.

In the summer of 2001, net evapotranspiration and its components were measured in a 125-year-old lodgepole pine stand in south central British Columbia<sup>14</sup>. Assuming a typical tree volume of 0.25 m<sup>3</sup> (ref. 15), the forest surface density was

20,000 m<sup>3</sup> km<sup>-2</sup>. Sapflow measurements suggested 31 mm mon<sup>-1</sup> of tree transpiration. Combined with rainfall, interception, soil moisture and soil composition measurements, the total inferred evapotranspiration was 74 mm mon<sup>-1</sup>. Adopting  $f_{live} = 1$  and  $\Sigma_0 / \Sigma_{crown} = 20,000 \text{ m}^3 \text{ km}^{-2} / 13,000 \text{ m}^3 \text{ km}^{-2}$  in equation (1), these stand-level results suggest  $E_{canopy,max} = 39 \text{ mm mon}^{-1}$  and  $E_{evap} = 42 \text{ mm mon}^{-1}$ , in agreement with the MODIS results to within 20%.

**MODIS latent heat loss satisfies a closed energy balance.** The reduction in latent heat flux post-disturbance is expected to raise daytime surface temperature, as solar energy previously spent evaporating water now heats the surface. The energy balance at the surface is maintained by increasing surface temperature, which in turn increases both the outgoing convective and radiative fluxes to fully compensate for the loss of latent heat flux.

Night-time evapotranspiration is small such that increases in minimum daily temperatures are negligible<sup>11,16</sup>, and the post-disturbance change to the diurnal temperature range can be used to independently estimate the corresponding decrease in transpiration (see Methods). Keeping only first-order terms, the perturbed energy balance predicts the post-disturbance change in  $E$  from that in  $T_{11} - T_{21}$  according to:

$$\Delta E \simeq -\frac{c_T}{c_E} \left( 4\sigma (T_s + 273.15)^3 + \frac{\rho C_p}{r_a} (1 - m) \right) \Delta (T_{11} - T_{21}) \quad (2)$$

Here,  $\sigma$  is the Stefan–Boltzmann constant ( $5.67 \times 10^{-8} \text{ W m}^{-2} \text{ K}^{-4}$ ),  $T_s$  is the daily average surface temperature (°C),  $\rho$  is the density of air ( $\text{kg m}^{-3}$ ),  $C_p = 1,005 \text{ J kg}^{-1} \text{ K}^{-1}$  is the heat capacity of air,  $r_a$  is the aerodynamic resistance to heat transfer ( $\text{s m}^{-1}$ ) and  $m$  is a constant near unity relating surface temperature to near-surface air temperature ( $m \equiv T_a / T_s$ ). The coefficients,  $c_E$  and  $c_T$ , account for the conversion from evaporative flux to latent heat flux and from the post-disturbance change in  $T_{11} - T_{21}$  to that in  $T_s$ , respectively. Equation (2) treats the surface as a blackbody and neglects potential post-disturbance changes to surface conduction, albedo and the incident radiative fluxes. Supplementary Information presents justification for these assumptions, as well as a full derivation of equation (2).

The coefficient in parentheses on the right-hand side of equation (2) has been measured through flux tower observations at twenty-two coniferous forest FLUXNET sites<sup>17</sup>. The mean value is  $4\sigma (T_s + 273.15)^3 + \rho C_p (1 - m) / r_a = 12.2 \text{ W m}^{-2} \text{ }^\circ\text{C}^{-1}$ ; the standard deviation is  $1.8 \text{ W m}^{-2} \text{ }^\circ\text{C}^{-1}$ . Assuming a sinusoidal diurnal temperature variation, and that post-disturbance changes to daily minimum temperatures are negligible,  $c_T / c_E$  can also be estimated (see Supplementary Information):  $c_T / c_E \approx 0.91 \text{ mm mon}^{-1} (\text{W m}^{-2})^{-1}$ . Thus, equation (2) suggests a linear relationship between  $\Delta (T_{11} - T_{21})$  and  $\Delta E$ , with an expected slope of approximately  $-11.1 \pm 1.6 \text{ mm mon}^{-1} \text{ }^\circ\text{C}^{-1}$ .

Figure 4c shows the analogue to Fig. 4a for  $T_{11} - T_{21}$ , binned as before in terms of  $\Sigma_0$  and  $f_{live}$ . For most stands ( $\Sigma_0 \gtrsim 11,000 \text{ m}^3 \text{ km}^{-2}$ ), Fig. 4a and c mirror each other, suggesting a linear relationship between  $\Delta (T_{11} - T_{21})$  and  $\Delta E$ , in accordance with equation (2). To test the predicted slope, post-disturbance changes in  $\Delta E$  and  $\Delta (T_{11} - T_{21})$  are calculated as the difference between the binned data points with  $f_{live} = 0.9-1.0$  (red curves in Fig. 4a,c) and the binned data points with  $f_{live} < 0.9$  (all other colours in Fig. 4a,c). Figure 4d shows the resulting differences plotted against each other for each  $\Sigma_0$  bin. For clarity, data with  $\Sigma_0 \leq 11,000 \text{ m}^3 \text{ km}^{-2}$  are not shown, as the linear relationship seems to break down in this low surface density regime.

The linear relationship between  $\Delta (T_{11} - T_{21})$  and  $\Delta E$  predicted by equation (2) is clear in Fig. 4d. The slope of the linear least-squares fit to all data points in Fig. 4d (black dashed line) is

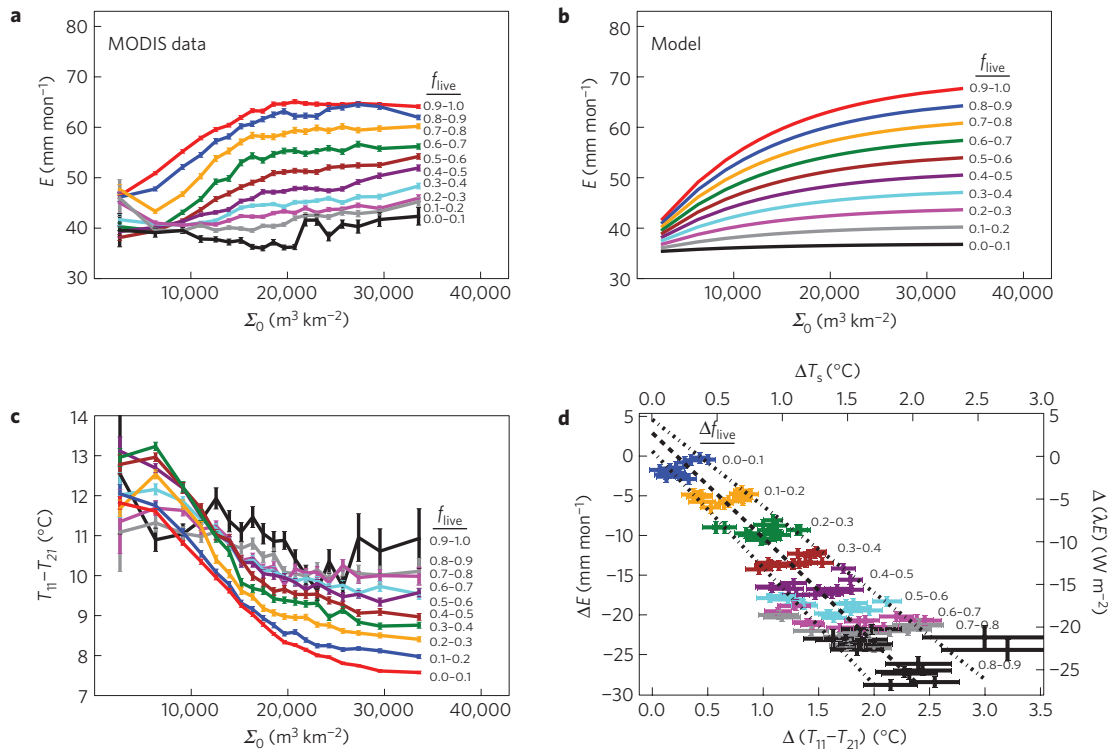


**Figure 4 | MODIS-observed variables as a function of initial forest surface density,  $\Sigma_0$ , and fraction of remaining live forest,  $f_{\text{live}}$ .** **a**, Evapotranspiration. **b**, A simple model for forest evapotranspiration with three free parameters fitted to the binned MODIS data. **c**, The MODIS day-night temperature difference. **d**, The observed change in the MODIS day-night temperature difference (from **c**) versus that in evapotranspiration (from **a**). The error bars in **a, c** are  $2\sigma$ , assuming the data contributing to each binned average are independent and those in **d** are propagated according to those shown in **a, c**.

$-13.2 \pm 0.5 \text{ mm mon}^{-1} \text{ } ^\circ\text{C}^{-1}$ . Thus, to within the errors, the fitted slope matches the expected slope for typical coniferous forests ( $-11.1 \pm 1.6 \text{ mm mon}^{-1} \text{ } ^\circ\text{C}^{-1}$ ), based on previously reported flux tower measurements. The linear relationship shows a modest dependency on initial forest surface density, probably owing to systematic variations in  $T_s$  and  $r_a$ . For comparison, the left and right dash-dotted lines in Fig. 4d represent linear fits to the lowest and highest initial surface density bins plotted.

In addition to allowing a closure test for the perturbed energy balance equation, the least-squares slope in Fig. 4d can be used to assess the relative contributions of post-disturbance enhancements in radiative and convective transport. The right and top axis labels in Fig. 4d represent the post-disturbance changes in latent heat flux and daily average surface temperature, respectively, where we have scaled the left and bottom axes by the aforementioned conversion factors:  $\Delta(\lambda E) = c_E \Delta E$  and  $\Delta T_s = c_T \Delta(T_{11} - T_{21})$ . The least-squares slope for these scaled variables is  $4\sigma(T_s + 273.15)^3 + \rho C_p(1 - m)/r_a = 14.5 \pm 0.6 \text{ W m}^{-2} \text{ } ^\circ\text{C}^{-1}$ , where the first and second terms in turn represent the temperature sensitivity of the outgoing radiative and convective fluxes. Adopting a typical stand temperature of  $T_s = 12^\circ\text{C}$  (see Supplementary Information), the blackbody sensitivity is  $4\sigma(T_s + 273.15)^3 \approx 5.3 \text{ W m}^{-2} \text{ } ^\circ\text{C}^{-1}$ . Subtracting this value from the least-squares slope, the inferred value for the convective sensitivity is  $\rho C_p(1 - m)/r_a \approx 9.2 \text{ W m}^{-2} \text{ } ^\circ\text{C}^{-1}$ . Thus, the partitioning of the fitted slope suggests that approximately one- and two-thirds of the latent heat flux lost post-disturbance is converted to outgoing radiative and sensible heat flux, respectively.

The regional impact of the beetle infestation in British Columbia can further be inferred by comparing Figs 1 and 4. Figure 1 suggests a typical decrease in forest surface density of 30% for all affected areas. In Fig. 4d, the average change in latent heat flux for  $\Delta f_{\text{live}} = 20\text{--}40\%$  is  $\Delta(\lambda E) = -10.4 \pm 0.3 \text{ W m}^{-2}$ , where the listed average includes the four low surface density bins not

shown, and the error represents the standard deviation in the mean, assuming the contributing values are independent. The corresponding average change in surface temperature is  $\Delta T_s = 1.00 \pm 0.03^\circ\text{C}$ . Referring to the convective sensitivity derived previously, the inferred increase in sensible heat flux is therefore  $\Delta H = 9.2 \pm 0.7 \text{ W m}^{-2}$ , where the listed error is dominated by uncertainties in the least-squares slope in Fig. 4d.

Averaged over all affected stands in all years considered, the mean latent heat flux is  $\lambda E = c_E E = 0.93 \text{ W m}^{-2}/(\text{mm mon}^{-1}) \times 58 \text{ mm mon}^{-1} = 54 \text{ W m}^{-2}$ . The fractional change in latent heat flux is therefore  $\Delta(\lambda E)/(\lambda E) = -10 \text{ W m}^{-2}/54 \text{ W m}^{-2} = -19\%$ . The fractional increase in sensible heat flux, on the other hand, is  $\Delta H/H \approx \Delta T_s/T_s = 1^\circ\text{C}/12^\circ\text{C} = 8\%$ , resulting in an increased Bowen ratio (the ratio of sensible to latent heat flux) of  $\Delta B/B \approx 27\%$ . The fractional increase in outgoing radiative flux is  $\Delta R/R \approx 4\Delta T_s/(T_s + 273.15) = 1\%$ . Note that the above results reflect mean changes, whereas the severity of the impact is highly variable. Referring to Fig. 4, the highest mortality areas affect fractional changes to the latent heat flux of  $\Delta(\lambda E)/(\lambda E) = -25 \text{ W m}^{-2}/54 \text{ W m}^{-2} = -46\%$ . The maximum surface temperature change of  $\Delta T_s = 2^\circ\text{C}$  results in increased radiative and sensible heat fluxes of 3% and 17%, respectively. The maximum Bowen ratio increase is 63%.

### Energy balance effects on other climate variables

Post-disturbance changes to the surface energy balance can have secondary impacts on regional climate. Heterogeneous land cover change, for example, induces contrasts in land surface temperature post-disturbance, which are observed in both measurement and simulation to significantly impact mesoscale circulations, cloud formation and precipitation<sup>18–21</sup>. Directly assessing the impact of the beetle infestation on each of these processes is beyond the scope of this work. However, the changes to the surface energy deduced

here can be compared to results for other types of disturbance in which secondary processes are known to be affected.

The changes to the latent and sensible heat fluxes we observe are comparable to those observed following wildfires, in which reported changes to the latent heat flux, sensible heat flux and Bowen ratio are  $\Delta(\lambda E)/(\lambda E) \approx -35\%$ ,  $\Delta H/H \approx 15\%$  and  $\Delta B/B \approx 50\%$ , respectively<sup>22</sup>. Regional modelling results of wildfires produce comparable changes to the surface energy balance<sup>23</sup>. Secondary changes in these simulations are also evident. For sufficiently large burned areas ( $>600 \text{ km}^2$ ), horizontal gradients in sensible heat flux drive mesoscale circulations, which further induce changes in the spatial and temporal distribution of cloud cover and precipitation in the region.

Although the observed consequences for sensible and latent heat flux are similar to those reported in the case of fire, the size of typical wildfires is much smaller than that of the present mountain pine beetle infestation. The meteorological consequences of this difference are not clear, as the scale of land cover heterogeneity is one of the primary drivers in determining the extent to which land cover changes are able to induce the mesoscale circulations that in turn impact cloud cover and precipitation. For scales smaller than a few kilometres, diffusion destroys the thermal gradients needed to drive mesoscale circulations affecting clouds and precipitation; scales greater than  $\sim 100 \text{ km}$ , on the other hand, cannot produce sufficient gradients in surface temperature. Heterogeneity scales of order  $10 \text{ km}$  are thought to be optimal<sup>18,20,21</sup>. However, inferring the characteristic heterogeneity scales from Fig. 1 is not straightforward. Land cover change in the case of insect infestation is less well ordered than in other types of disturbance, because both the scale of the impacted areas and the level of mortality within affected areas are variable. Future work is needed to understand the circumstances under which patchy and variable forest mortality drive significant secondary changes in regional climate.

## Methods

**Data and processing.** We employ the following data sets.

Annual forest and pine volume surface density, 1999–2010, 400-m grid, British Columbia Forest Survey<sup>1</sup> (<ftp://ftp.for.gov.bc.ca/hre/external/publish/web/BCMPB/>): densities represent the standing volume per unit area for trees with diameters  $\geq 12.5 \text{ cm}$  at breast height. Data combine forest cover inventory, management information and provincial aerial overview data. For comparison to MODIS, we fill each 1-km MODIS pixel with the area-weighted average of each contributing 400-m forest survey pixel. We analyse only pixels in which no more than 20% of MODIS pixel area is missing in the corresponding inventory data.

Monthly evapotranspiration, 2000–2010, 1-km grid, MODIS product MOD16 (refs 24,25) (<http://www.ntsug.umt.edu/project/mod16/>): retrieval is based on the Penman–Monteith equation, and uses MODIS leaf area index, land cover and albedo for characterizing the vegetation. Meteorological data from the Global Modelling and Assimilation Office reanalysis supply the remaining inputs.

Eight-day land surface temperature, 2000–2010, 1-km grid, MODIS product MOD11A2 (refs 26,27) (<ftp://ladsweb.nascom.nasa.gov/allData/5/>). Data are derived from radiance measurements in the thermal infrared bands processed according to land cover and the atmospheric temperature and water vapour profiles. Before seasonal averaging, we fill cloud-contaminated and missing data using linear interpolation between data available at adjacent time steps. We also exclude bad data in 2007 not originally flagged by the quality algorithm (Z. Wan, private communication, January 2012).

Sixteen-day white-sky albedo, 2000–2010, 1-km grid, MODIS product MCD43B3 (refs 28–30; <ftp://e4ftl01.cr.usgs.gov/MOTA/MCD43B3.005/>): data are retrieved by inverting multi-band surface reflectance observations. We again use linear interpolation to fill quality-flagged data.

Monthly precipitation, 2000–2009, 0.5° grid, GPCP Full Data Reanalysis product (version 5; refs 31,32; <http://gpcc.dwd.de/>): this is a station product appropriate for water balance studies. For comparison to MODIS, we assign each 1-km MODIS pixel the precipitation value associated with its overlying, coarser-resolution GPCP pixel.

Monthly terrestrial water storage, 2002–2010, 1° grid, GRACE (ref. 33; <http://grace.jpl.nasa.gov/data/gracemonthlymassgridsland/>): gravimetrically based GRACE land data are processed by S. Swenson through the NASA MEASURES

Program. The nominal resolution is 300 km, set by a Gaussian filter applied to the data during processing. A scaling grid computed from the Community Land Model has been applied to the data to restore flux removed by filtering.

Monthly river discharge, 2000–2009, WSC (ref. 34; <ftp://arccf10.tor.ec.gc.ca/wsc/software/HYDAT/>): gauge data at Hope Station are used to calculate Fraser Basin-averaged runoff.

The MODIS data are vital to the results presented here. An assessment of MODIS data quality is therefore included in the Supplementary Information.

**Multi-pixel average time series.** For clarity, only pixels in which the maximum period of disturbance occurred over one year were used in the composite in Fig. 2. However, composites averaged over pixels with multiple years of disturbance yielded very similar results. Confirming the visual impression, post-disturbance changes in Fig. 2 are statistically significant; application of a Student's *t*-test showed the four-year pre- and post-disturbance means to be discrepant at 99% confidence for all time series.

The time series in Fig. 2 further suggest that the observed changes are very unlikely to be caused by large-scale shifts in climatic variables such as temperature and precipitation. The multi-year compositing technique helps isolate the effects of disturbance from natural climatic fluctuations, which tend to be comparable to or greater than the observed changes following disturbance. Moreover, Fig. 1 shows that the level of mortality is highly heterogeneous. The observed post-disturbance changes in  $E$  and  $T_{11} - T_{21}$  are, on the other hand, segregated by level of mortality rather than by spatial location.

**Summertime precipitation limit on evaporation.** Whereas trees draw on deep stored water from winter and spring, the water evaporated from shallow soil layers and vegetation may not exceed the water supply provided by summertime precipitation. The MODIS algorithm calculates evaporation based on atmospheric pressure, temperature and humidity supplied by reanalysis, and thus does not explicitly use precipitation. As a consistency check, we therefore compare GPCP summertime precipitation to evaporation suggested by the MODIS product. Averaged over all MODIS pixels for all years with coincident GPCP data (2000–2009), the implied summertime precipitation is  $49 \pm 4 \text{ mm mon}^{-1}$ , which exceeds MODIS-derived summertime evaporation by approximately  $10\text{--}15 \text{ mm mon}^{-1}$ . The MODIS evaporative component of evapotranspiration is therefore consistent with this continuity constraint.

**Independence of MODIS evapotranspiration and surface temperature.** The MODIS evapotranspiration and land surface temperature retrievals are derived from largely independent data. MODIS evapotranspiration takes 1° reanalysis average surface temperature as an input. However, observed changes at the 1 km scale averaged over multiple years are driven by changes in remotely sensed leaf area, derived from observations in the optical and near-infrared. MODIS retrievals of surface temperature, on the other hand, are based on thermal infrared measurements. Differencing the daytime and night-time measurements further has the effect of removing systematic regional and interannual variations such that local, post-disturbance changes are readily apparent (Fig. 2).

Received 18 September 2012; accepted 23 October 2012;  
published online 25 November 2012

## References

- Walton, A. *Provincial-level Projection of the Current Mountain Pine Beetle Outbreak: Update of the Infestation Projection Based on the 2010 Provincial Aerial Overview of Forest Health and Revisions to the Model (BCMPB. v8)* (Ministry of Forests and Range, Research Branch, 2011).
- Hicke, J. A. & Jenkins, J. C. Mapping lodgepole pine stand structure susceptibility to mountain pine beetle attack across the western United States. *For. Ecol. Manag.* **255**, 1536–1547 (2008).
- Macias Fauria, M. & Johnson, E. Large-scale climatic patterns and area affected by mountain pine beetle in British Columbia, Canada. *J. Geophys. Res.* **114**, G01012 (2009).
- Bale, J. *et al.* Herbivory in global climate change research: Direct effects of rising temperature on insect herbivores. *Glob. Change Biol.* **8**, 1–16 (2002).
- Bentz, B. *et al.* Climate change and bark beetles of the western United States and Canada: Direct and indirect effects. *BioScience* **60**, 602–613 (2010).
- Kurz, W. *et al.* Mountain pine beetle and forest carbon feedback to climate change. *Nature* **452**, 987–990 (2008).
- Boon, S. Snow ablation energy balance in a dead forest stand. *Hydrol. Processes* **23**, 2600–2610 (2009).
- Rex, J., Dubé, S. *Hydrologic Effects of Mountain Pine Beetle Infestation and Salvage Harvesting Operations*. Mountain Pine Beetle Initiative Working Paper (Pacific Forestry Centre, 2009).
- Schnorbus, M. *A Synthesis of the Hydrological Consequences of Large-scale Mountain Pine Beetle Disturbance*, Mountain Pine Beetle Initiative Working Paper (Pacific Forestry Centre, 2011).

10. Varhola, A., Coops, N. C., Weiler, M. & Moore, R. D. Forest canopy effects on snow accumulation and ablation: An integrative review of empirical results. *J. Hydrol.* **392**, 219–233 (2010).
11. Vinukollu, R., Wood, E., Ferguson, C. & Fisher, J. Global estimates of evapotranspiration for climate studies using multi-sensor remote sensing data: Evaluation of three process-based approaches. *Rem. Sens. Environ.* **115**, 801–823 (2011).
12. Wang, K. & Dickinson, R. A review of global terrestrial evapotranspiration: Observation, modelling, climatology, and climatic variability. *Rev. Geophys.* **50**, RG2005 (2012).
13. Schmid, J. *Net precipitation within small group infestations of the mountain pine beetle*, Vol. 508 (USDA Forest Service, Rocky Mountain Forest and Range Experiment Station, 1991).
14. Spittlehouse, D. *Proc. 25th Conf. on Agricultural and Forest Meteorology* (American Meteorological Society, 2002).
15. Harris, J., Centre, P. F. R., Dawson, A. & Brown, R. *Evaluation of Mountain Pine Beetle Damage Using Aerial Photography: Flathead River, B.C., 1980* Information report (Canadian Forestry Service, 1982)..
16. Wiedinmyer, C., Barlage, M., Tewari, M. & Chen, F. Meteorological impacts of forest mortality due to insect infestation in Colorado. *Earth Interact.* **16**, 1–11 (2012).
17. Wilson, K. *et al.* Energy partitioning between latent and sensible heat flux during the warm season at FLUXNET sites. *Wat. Resour. Res.* **38**, 1294 (2002).
18. Mölders, N. *Land-Use and Land-Cover Changes* (Springer, 2012).
19. Bonan, G. Forests and climate change: forcings, feedbacks, and the climate benefits of forests. *Science* **320**, 1444–1449 (2008).
20. D'Almeida, C. *et al.* The effects of deforestation on the hydrological cycle in Amazonia: A review on scale and resolution. *Int. J. Clim.* **27**, 633–647 (2007).
21. Pielke, R. Influence of the spatial distribution of vegetation and soils on the prediction of cumulus convective rainfall. *Rev. Geophys.* **39**, 151–178 (2001).
22. Amiro, B., MacPherson, J. & Desjardins, R. BOREAS flight measurements of forest-fire effects on carbon dioxide and energy fluxes. *Agric. For. Meteorol.* **96**, 199–208 (1999).
23. Mölders, N. & Kramm, G. Influence of wildfire induced land-cover changes on clouds and precipitation in interior Alaska—A case study. *Atmos. Res.* **84**, 142–168 (2007).
24. Mu, Q., Heinsch, F., Zhao, M. & Running, S. Development of a global evapotranspiration algorithm based on MODIS and global meteorology data. *Rem. Sens. Environ.* **111**, 519–536 (2007).
25. Mu, Q., Zhao, M. & Running, S. Improvements to a MODIS global terrestrial evapotranspiration algorithm. *Rem. Sens. Environ.* **115**, 1781–1800 (2011).
26. Wan, Z. *MODIS Land-surface Temperature Algorithm Theoretical Basis Document (LST ATBD)* (Institute for Computational Earth System Science, 1999).
27. Wan, Z., Zhang, Y., Zhang, Q. & Li, Z. Quality assessment and validation of the MODIS global land surface temperature. *Int. J. Rem. Sens.* **25**, 261–274 (2004).
28. Wanner, W. *et al.* Global retrieval of bidirectional reflectance and albedo over land from EOS MODIS and MISR data: Theory and algorithm. *J. Geophys. Res.* **102**, 17143–17161 (1997).
29. Lucht, W., Schaaf, C. & Strahler, A. An algorithm for the retrieval of albedo from space using semiempirical BRDF models. *IEEE Trans. Geosci. Rem. Sens.* **38**, 977–998 (2000).
30. Schaaf, C. *et al.* First operational BRDF, albedo nadir reflectance products from MODIS. *Rem. Sens. Environ.* **83**, 135–148 (2002).
31. Rudolf, B. & Schneider, U. *Proc. 2nd Workshop of the Int. Precipitation Working Group IPWG 231–247* (2005).
32. Rudolf, B., Becker, A., Schneider, U., Meyer-Christoffer, A. & Ziese, M. *The New GPCP Full Data Reanalysis Version 5: Providing High-Quality Gridded Monthly Precipitation Data for the Global Land-Surface* GPCP Status Report December 2010 (2010).
33. Swenson, S. & Wahr, J. Post-processing removal of correlated errors in grace data. *Geophys. Res. Lett.* **33**, L08 (2006).
34. Environment-Canada. Water Survey of Canada: HYDAT Database National Water Data Archive (201–401 Burrard St., Vancouver, BC, V6C 3S5, 2011). <ftp://arccf10.tor.ec.gc.ca/wsc/software/HYDAT/>.

### Acknowledgements

This work was made possible by grants from the National Sciences and Engineering Research Council of Canada. We acknowledge valuable exchanges with G. Bonan, S. Déry, S. Dubé, P. Lawrence, P. Link, D. Moore, J. Oyler, S. Running, M. Schnorbus, A. Swann, S. Swenson, A. Varhola and Z. Wan.

### Author contributions

I.F. initially conceived the project. H.M. refined the scope of the project, designed and implemented the analysis methods, and wrote the paper. P.J.K. helped brainstorm ideas throughout this process. Both I.F. and P.J.K. contributed suggestions to several early drafts of the manuscript.

### Additional information

Supplementary information is available in the online version of the paper. Reprints and permissions information is available online at [www.nature.com/reprints](http://www.nature.com/reprints). Correspondence and requests for materials should be addressed to H.M.

### Competing financial interests

The authors declare no competing financial interests.